UNPAD

Vol. 10, No. 02 (2026) 138 – 154
JIIF (Jurnal Ilmu dan Inovasi Fisika)
https://jurnal.unpad.ac.id/jiif/

SINTA 3

EFFECT OF ANNEALING TEMPERATURE ON ZNO PROPERTIES FOR CO_2 REDUCTION

TRI KOMALA JUNITA[1,3], ERSIKA MORI[2], ABEL RAYHAN[2], KAYLA PUTRI HENDRAWAN[2], ANNISA APRILIA[2], FERRY FAIZAL[2,3], FITRILAWATIB[2,3,*]

[1]*Department of Biotechnology, Faculty of Graduate School, Padjadjaran University, Bandung 40132, Indonesia.*
[2]*Department of Physics, Faculty of Mathematics and Natural Sciences, Padjadjaran University, Sumedang 45363, Indonesia.*
[3]*Functional Nano Powder University Center of Excellence (FiNder U CoE), Universitas Padjadjaran, Jalan Raya Bandung-Sumedang KM 21, Jatinangor, Sumedang 45363, West Java, Indonesia*

**Corresponding author*
Email: fitrilawati@gmail.com

Submitted: 20/05/2026
Accepted: 25/06/2026
Published: 08/07/2026

Abstract. Zinc oxide (ZnO) is a promising semiconductor material for photoelectrochemical CO_2 reduction due to its favorable optoelectronic properties. In this study, ZnO was synthesized via the sol-gel method with varying thermal treatments: without annealing and with annealing at 150°C, 300°C, and 450°C under an inert nitrogen (N_2) atmosphere to investigate the evolution of structural and defect states. X-ray diffraction (XRD) patterns confirmed that all samples retained the hexagonal wurtzite structure, with crystallite size increasing systematically from 3.23 nm to 19.33 nm as the annealing temperature rose. Fourier-transform infrared (FTIR) spectroscopy revealed progressive surface dehydroxylation and identified residual bridging carboxylate and weakly bound acetic acid molecules from the precursor at 1582 cm^{-1} and 1340 cm^{-1}, which were almost completely decomposed at 450°C. Scanning electron microscopy (SEM) images showed a transition toward more uniform quasi-spherical nanoparticles with increasing temperature, while a porous-like surface texture was qualitatively observed for the 450°C sample. Energy-dispersive X-ray spectroscopy (EDS) indicated a decrease in the atomic percentage of oxygen, suggesting the formation of oxygen vacancies (VO), which was further supported by the dominant green-yellow visible emission in photoluminescence (PL) spectra. UV-Vis measurements exhibited a marginal redshift in the optical band gap from 3.33 eV to 3.30 eV with increasing temperature, indicating suppressed radiative recombination due to defect states. Cyclic voltammetry (CV) tests in a CO_2-saturated electrolyte showed that the ZnO electrode annealed at 450°C exhibited a significantly increased cathodic current density from -0.0334 mA/cm^2 (dark) to -0.0747 mA/cm^2 (under UV illumination), indicating photoactivated CO_2 reduction processes. Nevertheless, quantitative product analysis is still required to comprehensively verify the specific reduction products formed.

Keywords: ZnO; sol-gel; annealing; photoelectrochemistry; CO_2 reduction; oxygen vacancies

Abstrak. *Seng oksida (ZnO) merupakan material semikonduktor yang menjanjikan untuk reduksi CO_2 fotoelektrokimia karena sifat optoelektroniknya yang menguntungkan. Dalam penelitian ini, ZnO disintesis melalui metode sol-gel dengan perlakuan termal yang bervariasi: tanpa anil dan dengan anil pada suhu 150°C, 300°C, dan 450°C di bawah atmosfer nitrogen (N_2) inert untuk*

DOI: https://doi.org/10.24198/jiif.v10i2.70746 *e-ISSN: 2549-7014*

menyelidiki evolusi struktur dan keadaan cacat. Pola difraksi sinar-X (XRD) mengkonfirmasi bahwa semua sampel mempertahankan struktur wurtzite heksagonal, dengan ukuran kristalit meningkat secara sistematis dari 3,23 nm menjadi 19,33 nm seiring dengan peningkatan suhu anil. Spektroskopi inframerah transformasi Fourier (FTIR) mengungkapkan dehidroksilasi permukaan progresif dan mengidentifikasi sisa karboksilat jembatan dan molekul asam asetat yang terikat lemah dari prekursor pada 1582 cm^{-1} dan 1340 cm^{-1}, yang hampir sepenuhnya terurai pada 450°C. Citra mikroskop elektron pemindaian (SEM) menunjukkan transisi menuju nanopartikel kuasi-bola yang lebih seragam dengan peningkatan suhu, sementara tekstur permukaan seperti pori diamati secara kualitatif untuk sampel 450°C. Spektroskopi sinar-X dispersi energi (EDS) menunjukkan penurunan persentase atom oksigen, menunjukkan pembentukan kekosongan oksigen (VO), yang selanjutnya didukung oleh emisi tampak hijau-kuning dominan dalam spektrum fotoluminesensi (PL). Pengukuran UV-Vis menunjukkan pergeseran merah marginal pada celah pita optik dari 3,33 eV menjadi 3,30 eV dengan peningkatan suhu, menunjukkan penekanan rekombinasi radiatif karena keadaan cacat. Pengujian voltametri siklik (CV) dalam elektrolit jenuh CO_2 menunjukkan bahwa elektroda ZnO yang dianil pada suhu 450°C menunjukkan peningkatan signifikan pada kerapatan arus katodik dari -0,0334 mA/cm² (gelap) menjadi -0,0747 mA/cm² (di bawah iluminasi UV), yang mengindikasikan proses reduksi CO_2 yang diaktifkan oleh cahaya. Meskipun demikian, analisis produk kuantitatif masih diperlukan untuk memverifikasi secara komprehensif produk reduksi spesifik yang terbentuk.

Kata kunci: *ZnO; sol-gel; anil; fotoelektrokimia; reduksi CO_2; kekosongan oksigen*

1. Introduction

The combustion of fossil fuels for energy generation releases massive amounts of carbon dioxide (CO_2) into the atmosphere, which is the primary driver of the greenhouse effect, global warming, and extreme climate change [1]. In response, carbon capture and utilization (CCU) technologies have been developed to capture and convert CO_2 into renewable energy sources, such as methane, ethanol, and formic acid [2,3]. Among the various CCU approaches, thermocatalytic conversion requires high activation energy and faces material stability challenges, while biological conversion using microorganisms is constrained by slow reaction kinetics. Photocatalytic conversion relies on photon excitation but is hindered by rapid electron hole recombination, and electrochemical reduction driven by an external potential demands substantial overpotentials. As an alternative, photoelectrochemical (PEC) reduction integrates the advantages of both photocatalysis and electrocatalysis by harnessing solar energy to minimize electrical energy consumption while simultaneously improving product selectivity [4].

Zinc oxide (ZnO) is a widely studied n-type semiconductor renowned for its direct band gap of 3.37 eV and high exciton binding energy of 60 meV, which enable efficient excitonic emission at room temperature [5]. Its piezoelectric properties arise from a non-centrosymmetric wurtzite structure. Furthermore, ZnO exhibits biocompatibility, as well as electrochemical and photochemical stability, making it an excellent candidate for photoelectrochemical CO_2 reduction applications [3]. However, its conversion efficiency is often limited by rapid photogenerated charge carrier recombination and a narrow light absorption range [6].

Annealing is a critical post-synthetic heat treatment that significantly influences the crystal structure, morphology, and surface defect states of materials [7]. While thermal annealing in an oxygen atmosphere can improve stoichiometry and eliminate certain defects, annealing in an oxygen-deficient or inert nitrogen (N_2) environment promotes the formation of oxygen vacancies (V_o) [8]. In recent years, these defect structures

particularly V_o have been recognized as an effective strategy to enhance electrochemical CO_2 reduction. The tunable electronic structure associated with V_o acts as shallow donor states that increase carrier density, modify local band bending, and promote the adsorption and activation of CO_2 and its intermediates on the catalyst surface [8].

Several previous studies have investigated the effect of annealing temperature on material properties and catalytic performance. Lim et al. examined the effect of annealing across a temperature range of 0-800°C and found that higher annealing temperatures systematically increase crystallite size, while oxygen vacancies emerge at lower temperatures [9]. Bui et al. reported that high-temperature annealing in an oxygen atmosphere significantly enhances piezoelectric performance [10]. Umar et al. prepared ZnO nanoparticles annealed at various temperatures for photocatalytic dye degradation, demonstrating the critical dependence of catalytic efficiency on the thermal treatment temperature [11].

Suguna et al. observed that increasing the annealing temperature led to larger crystallite sizes and a narrowing band gap, with ZnO annealed at 1000°C showing the best photocatalytic activity due to improved crystallinity and a higher concentration of oxygen vacancies [12]. Furthermore, Zong et al. developed a ZnO catalyst enriched with oxygen vacancies and grain boundaries, which exhibited high selectivity and electrocatalytic activity toward CO production, attributing this enhancement to the active sites and optimized electron transfer facilitated by V_o [8].

Despite these reports, a knowledge gap remains regarding the effect of annealing at moderate temperatures (below 500°C) under a nitrogen atmosphere on the physicochemical properties of ZnO and their correlation with photoelectrochemical performance for CO_2 reduction, particularly from the perspective of surface defect mechanisms and charge recombination. This study aims to synthesize ZnO nanoparticles via a facile sol-gel method, followed by annealing at various temperatures (150°C, 300°C, and 450°C) under a continuous nitrogen (N_2) flow, along with a non-annealed control. This comparative analysis is designed to explore the systematic evolution of material properties. Comprehensive characterization of the ZnO samples was performed to evaluate their physical, chemical, and optical characteristics, as well as to assess their performance and mechanistic pathways for photoelectrochemical CO_2 reduction. Ultimately, this research is expected to provide deeper insights into defect engineering for environmental and sustainable energy applications.

2. Research Methods

2.1 Materials

Zinc acetate dihydrate ($Zn(CH_3COO)_2 \cdot 2H_2O$, ≥99.0%), sodium hydroxide (NaOH, ≥98.0%), and n-hexane (≥95.0%) were procured from Sigma-Aldrich. Methanol (≥99.8%) was supplied by Merck. Distilled water was obtained from an in-house purification system (PT Ikapharmindo Putramas, Indonesia). ITO-coated glass substrates (7 Ω/sq) were purchased from Xin Yan Technology. All chemicals were of analytical reagent grade and employed without additional purification.

2.2 Synthesis of ZnO Powder

$Zn(CH_3COO)_2 \cdot 2\ H_2O$ (1 g) was dissolved in methanol (42 mL) and stirred at 65°C, 250 rpm. NaOH solution (0.28 g in 23 mL methanol) was added slowly after sonicating for 15 minutes. The mixture was stirred for ±90 min, then aged for 2 days until a precipitate formed. The precipitate was purified with methanol and n-hexane (1:1) by centrifugation (3600 rpm, 10 min, 3 times) and dried in a vacuum oven for 12 hours. ZnO powder was calcined at 150°C, 300°C, and 450°C for 1 hour in a tube furnace with nitrogen gas.

2.3 Preparation of ZnO Thin-Film Electrode

ZnO powder (40 mg) was dispersed in absolute ethanol (40 mL) by magnetic stirring at 250 rpm for 3 hours at room temperature, followed by bath ultrasonication for 30 minutes. ITO substrates were sequentially cleaned in distilled water, ethanol, and isopropanol under ultrasonication at 40 °C for 15 minutes each and dried with N_2 gas. The ZnO suspension was spray-coated onto the substrates at 50 °C using air carrier gas at 45 psi; 50 layers were deposited with a 1-minute interval between layers. The resulting films were annealed at 200 °C for 2 hours under flowing Argon gas and cooled to room temperature prior to use.

2.4 Photoelectrochemical Measurement

The photoelectrochemical performance of the ZnO thin-film electrodes was evaluated in a three-electrode H-type cell separated by a Nafion® 117 membrane (H^+ form). A platinum plate (1 × 3 cm^2) and an Ag/AgCl (saturated KCl) electrode served as the counter and reference electrodes, respectively. Potentials were reported vs. RHE. The electrolyte was 0.5 M Na_2SO_4 saturated with CO_2 (99%, 1 atm) by continuous bubbling for 15 min prior to and during measurements. CV was recorded at 10 mV s^{-1} from 0 to –2 V vs. RHE at ambient temperature. Measurements were performed under dark and UV illumination (λ = 365 nm, 10 mW cm^{-2}). The electrodes were preconditioned by repeated CV cycling until stable responses were achieved.

3. Results and Discussion

3.1 Structural Characterization by X-Ray Diffraction

The crystal structure and phase purity of the as-prepared ZnO samples were investigated by X-ray diffraction (XRD). Figure 1 shows the XRD patterns of the non-annealed ZnO (ZnO NA) and the ZnO samples annealed at 150 °C, 300 °C, and 450 °C (designated as ZnO 150, ZnO 300, and ZnO 450, respectively). All diffraction peaks can be unambiguously indexed to the hexagonal wurtzite structure of ZnO in excellent agreement with the reference database (COD 96-901-1663) [13]. No additional peaks corresponding to impurities or secondary phases were detected, indicating the high phase purity of all synthesized samples. The three dominant diffraction peaks observed at 2θ values of approximately 31.7°, 34.4°, and 36.2° correspond to the (100), (002), and (101) crystallographic planes, respectively, which are characteristic of the wurtzite structure. A systematic evolution in peak profile is clearly observed with increasing annealing temperature. Specifically, the diffraction peaks exhibit a progressive increase in intensity and a concomitant narrowing of their full width at half maximum (FWHM). These observations indicate a continuous improvement in crystallinity and a reduction in lattice disorder, which can be attributed to enhanced atomic mobility and grain growth during thermal annealing [13]. The absence of peak shifting further confirms that the Wurtzite

structure is preserved throughout the annealing process, with no detectable phase transformation.

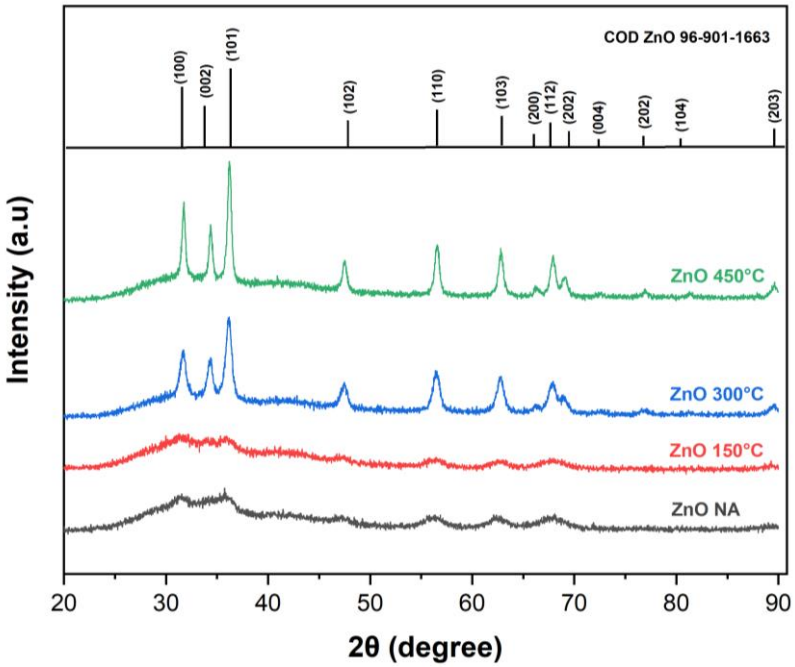

Figure 1. XRD patterns of non-annealed ZnO (ZnO NA) and ZnO samples annealed at 150°C, 300°C, and 450°C. The standard diffraction pattern for hexagonal wurtzite ZnO (COD 96-901-1663) is shown as reference.

The average crystallite size (D) of the ZnO nanoparticles was calculated from the dominant (101) diffraction peak using the Scherrer equation [14], where K is the shape factor (0.9), λ is the X-ray wavelength (0.15406 nm for Cu Kα), β is the full width at half maximum (FWHM) of the (101) peak, and θ is the Bragg angle. The calculated structural parameters are summarized in Table 1.

$$D = \frac{K\lambda}{\beta \cos\theta} \tag{1}$$

Table 1. FWHM and crystallite size data of ZnO

Sample	FWHM	Cristalite size (nm)
ZnO NA	2.58°	3.23
ZnO 150°C	1.89°	4.40
ZnO 300°C	0.72°	11.53
ZnO 450°C	0.43°	19.33

The crystallite size increased systematically from 3.23 nm to 19.33 nm, accompanied by a dramatic narrowing of the FWHM, which is driven by the supply of external thermal energy during calcination [15]. This thermal energy provides sufficient kinetic activation energy for the solid-state diffusion of zinc and oxygen ions, allowing them to migrate from highly disordered, amorphous boundaries into the periodic hexagonal wurtzite lattice coordinates [9,10]. This thermal treatment may facilitate the relaxation of internal stress and structural dislocations up to a certain temperature threshold [9,10]. Furthermore, this ordered grain coalescence provides well-defined nucleation centers that minimize the nucleation energy barrier, promoting a relaxed and stoichiometrically balanced crystal

lattice [13]. This preferred vertical alignment along the (002) plane is highly advantageous for overall charge transport and optoelectronic functionality [9,13]. However, while thermal treatment improves long-range structural order, annealing under a continuous nitrogen flow (an oxygen-deficient atmosphere) can simultaneously induce point defects. The desorption of lattice oxygen under inert conditions creates oxygen vacancies, which can introduce local microstrain and alter the electronic properties. Therefore, high crystallinity from XRD does not necessarily indicate a defect-free lattice [9,10].

3.2 FTIR Spectroscopy

The surface chemical composition and functional groups of the synthesized ZnO samples were characterized by Fourier-transform infrared (FTIR) spectroscopy. Figure 2 shows the FTIR spectra of the non-annealed ZnO (ZnO NA) and the ZnO samples annealed at 150°C, 300°C, and 450°C (ZnO 150, ZnO 300, and ZnO 450, respectively) recorded in the wavenumber range of 400-4000 cm. All samples exhibited a broad absorption band centered between 3408 and 3446 cm^{-1}, which is attributable to the O–H stretching vibrations of surface-adsorbed water molecules and hydroxyl (–OH) groups. This band gradually decreased in intensity with increasing annealing temperature, indicating progressive dehydroxylation of the ZnO surface upon thermal treatment.

Two distinct absorption peaks were observed at approximately 1582 cm^{-1} and 1340 cm^{-1} in the spectra of the non-annealed and low-temperature-annealed samples. The peak at 1582 cm^{-1} is assigned to the asymmetric stretching vibration of carboxylate groups (COO^-) in a bridging bidentate coordination mode (M–OCOO–M), while the peak at 1340 cm^{-1} corresponds to the symmetric stretching vibration of carboxylate species or the C–O stretching mode of weakly adsorbed acetic acid (CH_3COOH) originating from the zinc acetate precursor [2,3]. Additionally, a relatively weak absorption band was detected at approximately 1026 cm^{-1} (with slight variations at 1022, 1024, 1022, and 1020 cm^{-1} across samples), which can be assigned to the C–O stretching vibration of carboxyl bonds. This feature is likely derived from carbonate species or residual carbonaceous intermediates formed during the synthesis process [12,14].

For the non-annealed (ZnO NA) and 150 °C-annealed samples, a characteristic bending vibration of Zn–OH was observed at approximately 900 cm^{-1}. This peak was completely absent in the spectra of the samples annealed at 300 °C and 450 °C, indicating complete surface dehydroxylation [15,16]. The thermal treatment provides sufficient energy to drive a condensation reaction between adjacent surface-bound hydroxyl groups, as described by the following equation [17].

$$2\ Zn\text{-}OH \rightarrow Zn\text{-}O\text{-}Zn + H_2O\ (g) \quad (2)$$

This dehydroxylation process converts weakly bound surface species into rigid, highly coordinated Zn–O–Zn network bonds. This structural transformation is reflected by the progressive sharpening and increased definition of the characteristic Zn–O lattice stretching bands observed in the 450–667 cm^{-1} region [15–17]. The emergence of well-defined Zn–O–Zn stretching modes between 415 and 520 cm^{-1} confirms the formation of crystalline ZnO, indicating a substantial transformation of the zinc acetate precursor into the oxide phase [12,14–16].

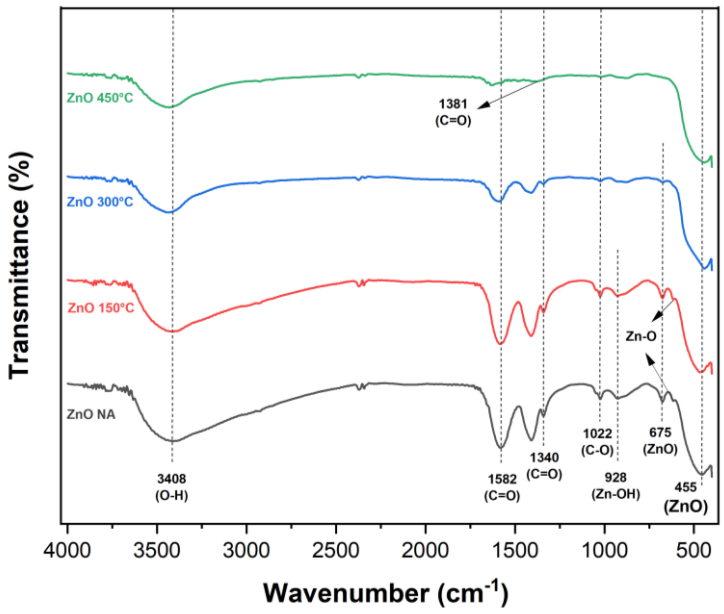

Figure 2. FTIR spectra of non-annealed ZnO (ZnO NA) and ZnO samples annealed at 150°C, 300°C, and 450°C recorded in the wavenumber range of 400–4000 cm^{-1}. Characteristic bands corresponding to O–H stretching (3408–3446 cm^{-1}), carboxylate bridging (1582 cm^{-1}), acetate/CH_3COOH (1340 cm^{-1}), and C–O stretching (~1026 cm^{-1}) are indicated.

Furthermore, as the annealing temperature was increased to 450 °C, the intensity of the residual acetate-related peaks at 1582 cm^{-1} and 1340 cm^{-1} decreased markedly, confirming the near-complete thermal decomposition of organic precursor residues [9]. In addition, the thermal treatment induced a blue shift of the vibrational mode near 539 cm^{-1}, which is associated with oxygen vacancies (V_o). This shift indicates a restructuring of the oxygen sublattice and provides further evidence for the evolution of defect states upon annealing [8,15].

3.3 Morphological and Elemental Analysis (SEM/EDS)

The surface morphology and particle distribution of the synthesized ZnO samples were examined by scanning electron microscopy (SEM). Figure 3 displays the SEM images of the non-annealed ZnO (ZnO NA) and the ZnO samples annealed at 150°C, 300°C, and 450°C (ZnO 150, ZnO 300, and ZnO 450, respectively) at 50,000× magnification. The non-annealed ZnO NA sample exhibited dense, irregular clusters on the nanometer scale (~100 nm), arising from the spontaneous agglomeration of ultra-small primary crystallites (3.23 nm) to minimize their high surface free energy [17]. For the ZnO 150 sample, grain boundaries began to emerge; however, large agglomerates remained evident. As the annealing temperature was increased to 300°C and 450°C, a more homogeneous distribution of particles with reduced apparent agglomerate size was observed, indicating thermally induced structural reorganization [15].

To quantitatively evaluate the morphological evolution, the apparent particle (agglomerate) size was estimated from SEM micrographs using ImageJ software based on the Feret diameter. The analysis yielded average sizes of 74.3 ± 15.2 nm, 43.1 ± 8.6 nm, and 32.5 ± 4.8 nm for the ZnO samples annealed at 150°C, 300°C, and 450°C, respectively (Table 2). The progressive decrease in average diameter, accompanied by a narrowing standard deviation, quantitatively confirms that thermal treatment promotes a more uniform and homogeneous nanoparticle distribution, consistent with thermally

induced grain growth [12,14,15]. Notably, the ZnO 450 sample displayed a rough surface texture, qualitatively suggesting a porous network architecture that could potentially enhance the electrochemically active surface area. However, as nitrogen physisorption (BET) analysis was not performed in this study, a definitive quantitative assessment of porosity and specific surface area cannot be established.

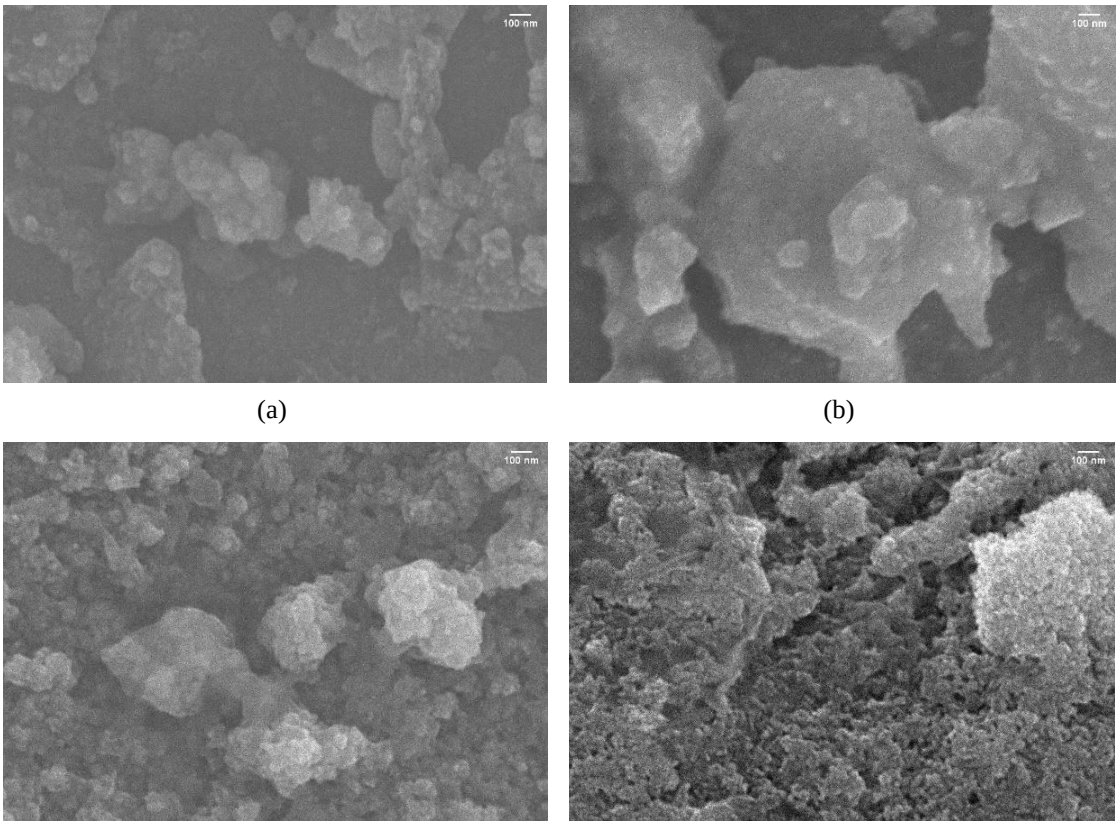

Figure 3. SEM images of (a) ZnO NA, (b) ZnO 150, (c) ZnO 300, and (d) ZnO 450 nanoparticles at 50,000× magnification.

Energy-dispersive X-ray spectroscopy (EDS) was performed to evaluate the elemental composition of the ZnO samples, and the results are summarized in Table 2.

Table 2. Atomic composition of sample materials ZnO NA, ZnO 150°C, ZnO 300°C and ZnO 450°C EDS test results

Sample Name	**Morphological Characteristics (SEM)**	**Apparent Particle Size (ImageJ, nm)**	**Atomic Percentage (%)**		**Atomic Ratio**
			Zn	**O**	**Zn : O**
ZnO NA	Dense, irregular agglomerates	~100 (cluster size)	52.69	47.31	1.11 : 1
ZnO 150°C	Reduced agglomeration, emerging grains	74.3 ± 15.2	58.95	41.05	1.44 : 1
ZnO 300°C	Semi-dispersed quasi-spherical particles	43.1 ± 8.6	52.81	47.17	1.12 : 1
ZnO 450°C	Homogeneous quasi-spherical, rough texture	32.5 ± 4.8	56.59	43.40	1.30 : 1

The EDS analysis revealed that the chemical composition of all synthesized samples deviated from the ideal 1:1 stoichiometry of bulk ZnO. Notably, the ZnO 450 sample exhibited a significant oxygen deficiency, as indicated by a nominal Zn:O atomic ratio of 1.30:1 (corresponding to $ZnO_{0.77}$). A decrease in the atomic percentage of oxygen with increasing annealing temperature is commonly associated with the formation of oxygen vacancies (V_o) during thermal treatment under an inert nitrogen atmosphere [14,15]. However, it is important to note that EDS is a semi-quantitative technique with inherent limitations in detecting light elements such as oxygen. Consequently, the EDS data alone cannot serve as definitive confirmation of oxygen vacancies. Rather, these results should be considered as an initial indication that requires verification through complementary techniques, such as photoluminescence (PL) spectroscopy, which are more sensitive to defect states.

3.4 UV-Vis Spectroscopy

UV-Vis spectroscopy was employed to investigate the optical properties and band gap evolution of the ZnO samples as a function of annealing temperature. Figure 4(a) shows the UV-Vis absorbance spectra of the non-annealed ZnO (ZnO NA) and the ZnO samples annealed at 150°C, 300°C, and 450°C (ZnO 150, ZnO 300, and ZnO 450, respectively). All samples exhibited distinct absorption edges in the UV region, characteristic of the wide band gap semiconductor nature of ZnO. With increasing annealing temperature, a systematic redshift of the absorption onset was observed, with the absorption peak shifting from approximately 346 nm (ZnO NA) to 358 nm (ZnO 450). The high absorbance values indicate that the materials possess strong light-harvesting capability in the UV region, which is favorable for photoelectrochemical applications [10].

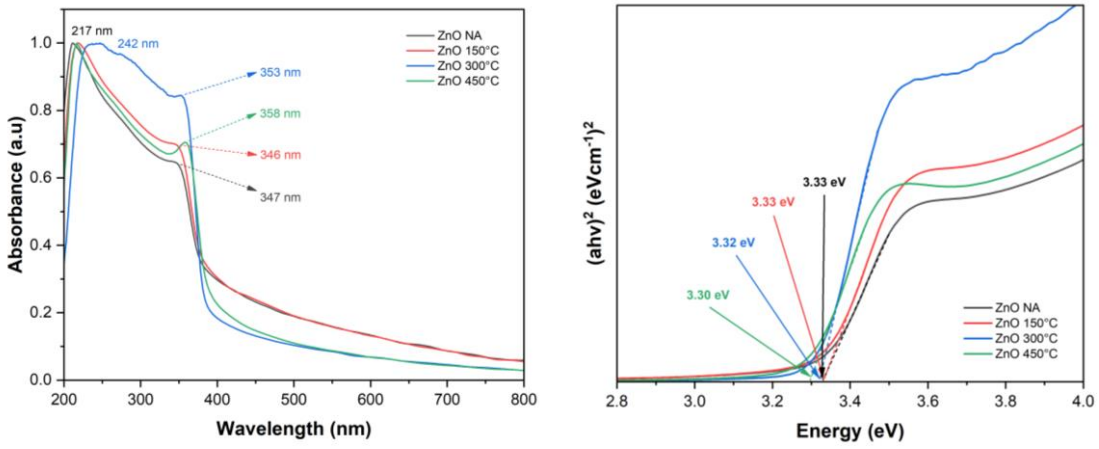

(a) (b)

Figure 4. (a) UV-Vis absorbance spectra and (b) Tauc plots for band gap determination of ZnO NA, ZnO 150, ZnO 300, and ZnO 450 samples.

To quantitatively determine the optical band gap, the Tauc plot method was employed [18]. Figure 4(b) presents the corresponding Tauc plots, from which the band gap energies were estimated to be 3.33 eV (ZnO NA), 3.33 eV (ZnO 150), 3.32 eV (ZnO 300), and 3.30 eV (ZnO 450). A marginal but consistent decrease in the band gap was observed as the annealing temperature increased to 450°C. This narrowing of the band gap is attributed to two competing effects: the growth of particle size and the reduction of material defects due to thermal treatment [19].

The thermal desorption of oxygen under an inert nitrogen flow generates oxygen vacancies (V_o), which introduce localized donor-like states in the sub-bandgap region (approximately 0.1–0.3 eV below the conduction band edge). These defect states can hybridize with the conduction band, thereby slightly lowering the optical transition threshold [8,9]. The observed band gap narrowing trend with increasing annealing temperature is well-documented in the literature and is governed by a combination of grain size, lattice parameters, and charge carrier concentration [12,19]. Overall, the UV-Vis results confirm that thermal annealing not only improves crystallinity but also modulates the electronic structure of ZnO through controlled defect engineering.

3.5 Photoluminescence Spectroscopy

To confirm the presence of oxygen vacancies and elucidate the photogenerated charge carrier dynamics, photoluminescence (PL) spectroscopy was performed at room temperature. Figure 5 presents the PL spectra of the non-annealed ZnO (ZnO NA) and the ZnO samples annealed at 150°C, 300°C, and 450°C (ZnO 150, ZnO 300, and ZnO 450), along with their deconvoluted peak components. The deconvoluted PL spectra reveal two primary emission features: (i) a sharp ultraviolet (UV) near-band-edge (NBE) emission centered at approximately 3.1 eV, corresponding to free exciton recombination, and (ii) a broad green–yellow deep-level emission (DLE) band spanning 500–600 nm (~2.0–2.2 eV), which is characteristic of defect-related radiative transitions [9].

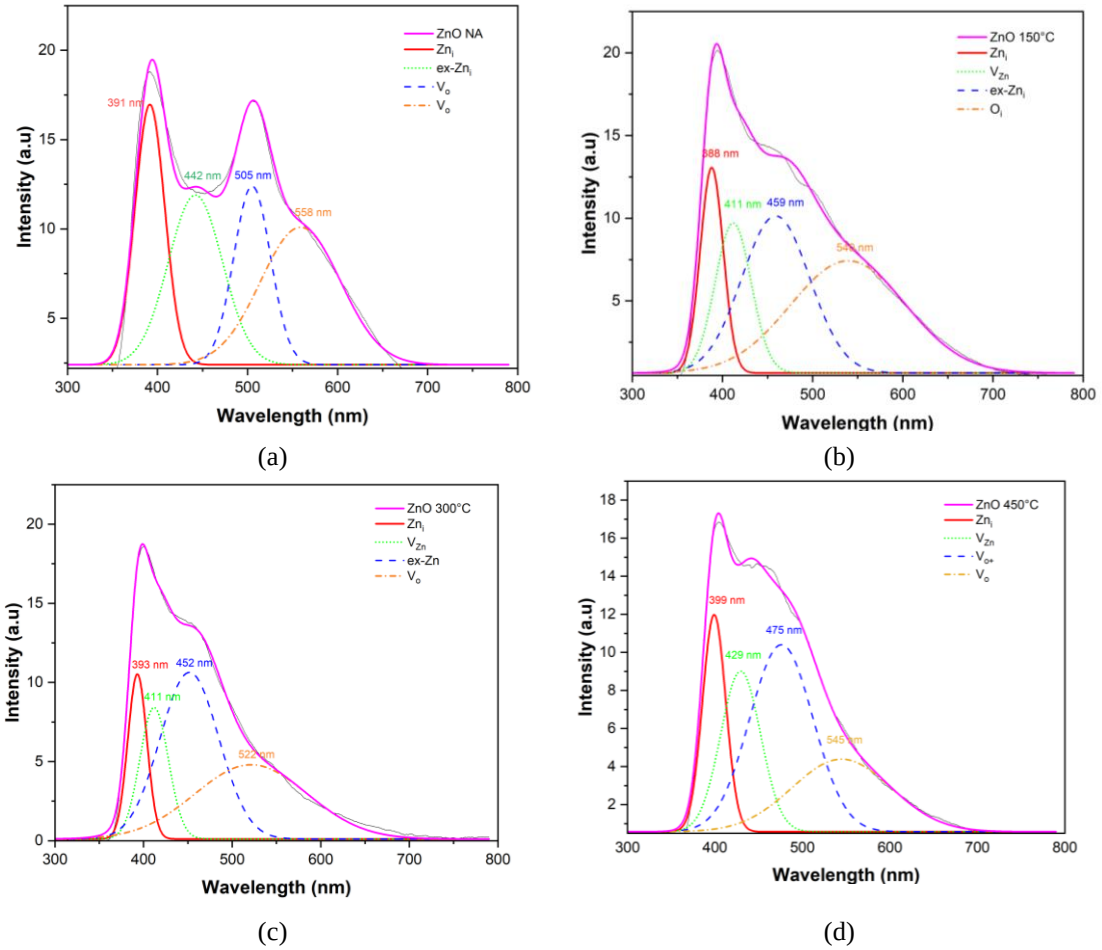

Figure 5. PL spectra with deconvoluted peak of (a) ZnO NA, (b) ZnO 150°C, (c) ZnO 300°C, and (d) ZnO 450°C nanoparticles.

The green-yellow visible emission is widely accepted in the literature as originating from the radiative recombination of photogenerated electrons (from the conduction band or shallow donor states) with holes trapped in ionized surface oxygen vacancies (V_o) [9]. The dominant green-yellow emission observed in the ZnO 450 sample provides strong, confirmative evidence of a high concentration of oxygen vacancies, thereby validating the initial indication derived from the EDS atomic ratio analysis. When ZnO is annealed under an inert N_2 atmosphere, the chemical gradient drives the thermal desorption of oxygen anions from the lattice without reoxidation, creating stable oxygen vacancy sites on the surface as shown in equation (3) [8,9].

$$O_o^x \rightarrow \frac{1}{2} O_2(g) + V_o^{++} + 2e^- \quad (3)$$

In highly crystalline systems such as ZnO 450, these surface oxygen vacancies act as efficient charge-trapping centers [8,9]. Upon UV excitation, photogenerated electrons are temporarily trapped in the localized mid-gap states, spatially separating them from the valence band holes. This trapping mechanism suppresses fast radiative recombination, thereby extending the lifetime of photogenerated charge carriers (e^-/h^+) and allowing more carriers to migrate to the catalyst/electrolyte interface [12,15]. The PL deconvolution clearly separates the excitonic NBE emission (~3.1 eV) from the oxygen-vacancy-related DLE emissions (~2.2 eV and ~2.0 eV), providing a quantitative marker for defect concentration [9,15]. Consequently, the prolonged carrier lifetime facilitates the migration of more electrons to the interface, where they can participate in the multi-electron CO_2 reduction reaction [8,20].

3.6 Photoelectrochemical Performance

The electrochemical behavior of the ZnO photoelectrodes (ZnO NA, ZnO 150, ZnO 300, and ZnO 450) was initially investigated in an N_2-saturated 0.5 M Na_2SO_4 electrolyte (in the absence of CO_2). As shown in Figure 6(a–d), the cyclic voltammetry (CV) curves exhibit a featureless, purely capacitive profile with no observable redox peaks. This confirms the absence of faradaic charge transfer at the electrode/electrolyte interface under these conditions; the recorded background current is attributed solely to double-layer charging and discharging processes [20]. Furthermore, the current densities in the N_2-saturated electrolyte are higher than those observed under CO_2-saturated conditions. This is because the photogenerated charge carriers are consumed exclusively for internal conduction toward the back contact, rather than being utilized in interfacial faradaic reactions. This behavior underscores the chemical stability and clean surface state of the ZnO electrodes in the inert aqueous electrolyte [17].

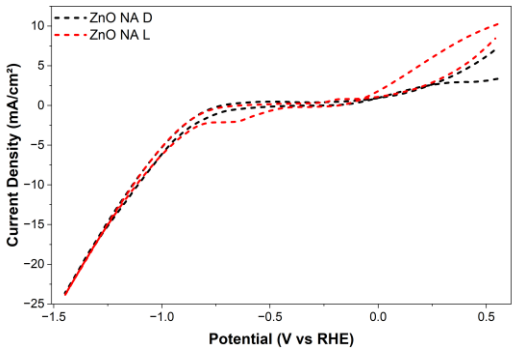

(a)

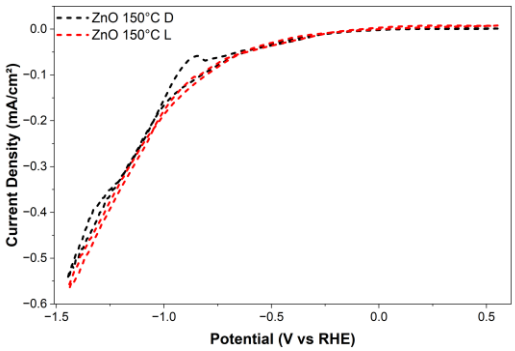

(b)

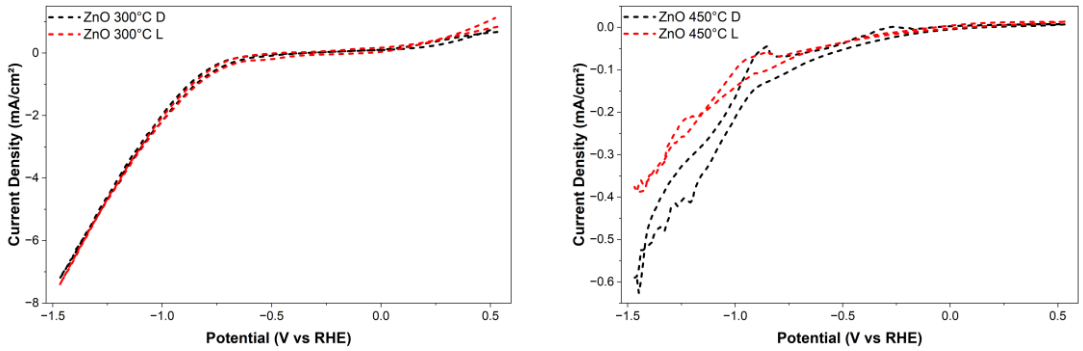

(c) (d)

Figure 6. Cyclic voltammetry curves recorded in N_2-saturated 0.5 M Na_2SO_4 (without CO_2) for (a) ZnO NA, (b) ZnO 150°C, (c) ZnO 300°C, and (d) ZnO 450°C electrodes.

To evaluate the CO_2 reduction activity, CV measurements were performed in a 0.5 M Na_2SO_4 electrolyte saturated with CO_2 (bubbling for 30 min). The resulting CV curves for all ZnO electrodes are presented in Figure 7(a–d). In contrast to the inert electrolyte, these curves exhibit distinct cathodic and anodic peaks, indicating the occurrence of electron transfer between the electrode and the dissolved CO_2, as well as hole transfer with the solution components at the cathode and anode, respectively [20].

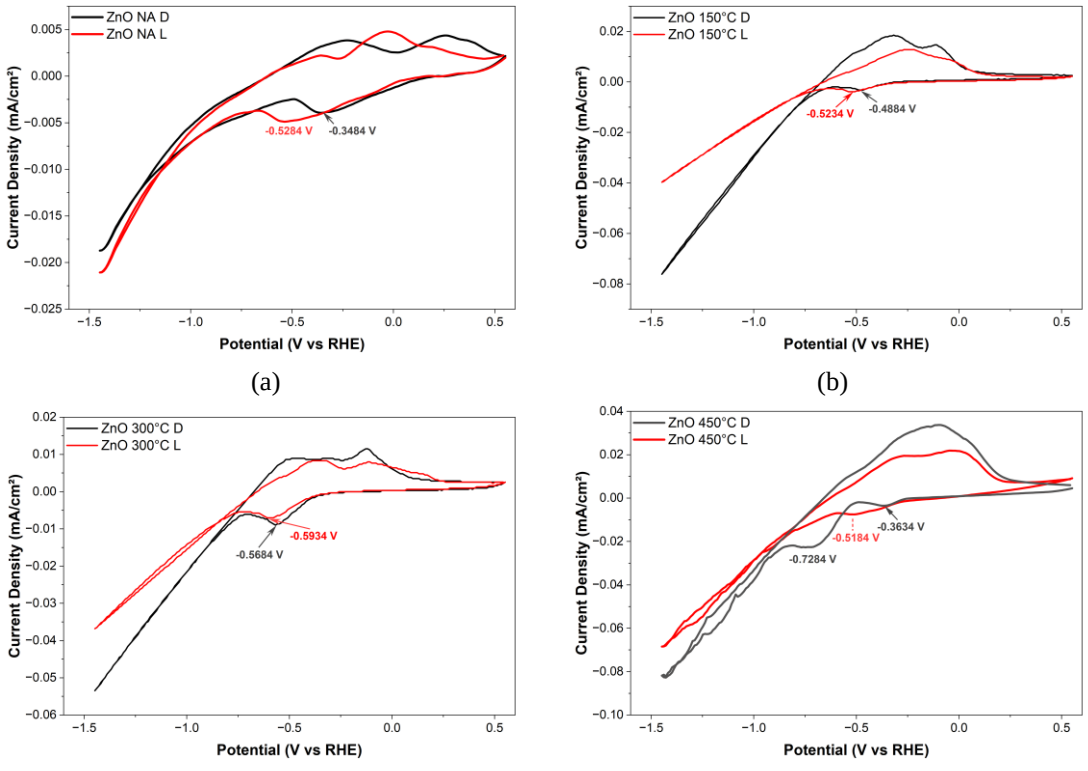

(a) (b)

(c) (d)

Figure 7. CV curves with CO_2 at electrodes (a) ZnO NA, (b) ZnO 150°C, (c) ZnO 300°C and (d) ZnO 450°C.

The key electrochemical parameters, including the cathodic peak potential (E_{pc}) and cathodic peak current density (I_{pc}), are summarized in Table 3. For the ZnO NA and ZnO 150 electrodes (Figures 7a and 7b), the cathodic peak current densities are notably low, with negligible differences between dark and illuminated conditions. This behavior is ascribed to their small crystallite sizes (3.23 nm and 4.40 nm, respectively). The high

density of grain boundaries in these samples acts as efficient recombination centers, trapping and annihilating photogenerated electron-hole pairs, thus limiting the faradaic current [20].

Table 3. Cathodic peak potential ((*E*$_{pc}$) and peak current density (*I*$_{pc}$) for ZnO NA, ZnO 150, ZnO 300, and ZnO 450 electrodes under dark and UV illumination.

Sample Name		$\mathbf{E_{pc1}}$ $(\mathbf{V\ vs.\ RHE})$	$\mathbf{I_{pc1}}$ $(\mathbf{mA/cm^2})$	$\mathbf{E_{pc2}}$ $(\mathbf{V\ vs.\ RHE})$	$\mathbf{I_{pc2}}$ $(\mathbf{mA/cm^2})$
ZnO NA	Dark	-0.3484	-0.039		
	Light	-0.5284	-0.0486		
ZnO 150°C	Dark	-0.4884	-0.0325		
	Light	-0.5234	-0.0387		
ZnO 300°C	Dark	-0.5684	-0.0881		
	Light	-0.5934	-0.0709		
ZnO 450°C	Dark	-0.3634	-0.0334	-0.7284	-0.02255
	Light	-0.5184	-0.0747		

The ZnO 300 electrode displays a distinctive voltammetric response, exhibiting a higher cathodic peak current density under dark conditions (I_{pc1} = -0.0881 mA cm^{-2}) compared to under UV illumination (I_{pc1} = -0.0709 mA cm^{-2}). This anomalous behavior, where the dark current exceeds the photocurrent, can be rationalized by a comprehensive analysis of the material's physicochemical properties. Structurally, the annealing process at 300°C resulted in a significant increase in crystallite size (11.53 nm), substantially reducing the grain boundary density and the internal charge transfer resistance. This facilitates a higher dark faradaic current compared to the ZnO NA and ZnO 150 electrodes [14]. The FTIR analysis further supports this, showing complete dehydroxylation (loss of the Zn-OH band at ~900 cm^{-1}) and the formation of a rigid, highly conductive Zn–O–Zn network [15].

Crucially, while the organic residues are largely eliminated at 450°C, the ZnO 300 sample retains prominent features corresponding to bridging carboxylates (~1582 cm^{-1}) and weakly bound acetic acid (~1340 cm^{-1}) [9,21]. These deprotonated carboxylate/acetate species on the surface are proposed to act as electroactive surface states or donor sites in the dark. They facilitate the coordination and polarization of incoming CO_2 molecules at the interface, thereby enhancing the dark faradaic current. Morphologically, the presence of well-dispersed, quasi-spherical agglomerates with an apparent size of 43.1 ± 8.6 nm provides a homogeneous surface area that ensures stable electrochemical contact with the electrolyte [15]. The slight decrease in cathodic current under UV illumination (to -0.0709 mA cm^{-2}) is attributed to the wide band gap (3.32 eV), which limits the photovoltage, combined with a relatively low concentration of oxygen vacancies (V_o). The low V_o concentration, evidenced by a nominal Zn:O ratio of 1.12:1 and a weak green-yellow emission band in the PL spectrum [9,17], minimizes charge-trapping states. Consequently, photogenerated electron-hole pairs undergo rapid recombination, particularly at the remaining organic/acetate impurity sites [9,12]. Additionally, UV illumination may induce photo-desorption or photochemical alteration of these electroactive acetate surface states, reducing the density of active sites for CO_2 adsorption and further suppressing the photoresponse [9,15].

For the ZnO 450 electrode, a significant photo-enhancement was observed. Under dark conditions, the cathodic peak current density (I_{pc1}) was -0.0334 mA cm^{-2}. Upon UV illumination, this value increased substantially to -0.0747 mA cm^{-2} (Table 3). This

enhancement confirms the effective contribution of photogenerated electrons migrating to the electrode surface, facilitated by suppressed recombination and an increased concentration of surface oxygen vacancies, which is consistent with previous reports [20].

The significant cathodic shift in peak potentials observed for all electrodes in the CO_2-saturated electrolyte is governed by two primary interfacial phenomena First, the dissolution of CO_2 in the unbuffered 0.5 M Na_2SO_4 electrolyte forms carbonic acid (H_2CO_3), lowering the bulk pH to approximately 4–5 [20,22]. Upon applying a negative cathodic bias, the rapid consumption of protons (H^+) at the electrode surface, driven by the competing hydrogen evolution reaction (HER) and CO_2 reduction, exceeds the proton diffusion rate from the bulk [3]. This results in severe local proton depletion, causing the local surface pH to rise to highly alkaline values (pHlocal > 9) [17,20].

$$E = E^0 - 0.0591 \times \text{pH} \quad (4)$$

According to the Nernst equation (Eq. 24), this dramatic local pH increase shifts the thermodynamic reduction potentials of all CO_2 reduction pathways to significantly more negative values, accounting for the observed cathodic shift in the CV scans [20]. Second, the activation polarization of the CO_2 molecule plays a critical role. The linear, centrosymmetric CO_2 molecule is highly stable due to its strong, non-polar C=O double bonds (~750 kJ mol^{-1}). The single-electron transfer required to bend the molecule into a radical anion ($CO_2^{\cdot -}$) is energetically unfavorable, requiring an extremely negative potential of -1.90 V vs. SHE [2,23]. This substantial thermodynamic barrier induces a strong activation polarization, forcing the cathodic current to onset at highly negative overpotentials [20].

While the occurrence of these cathodic peaks in the CO_2 saturated electrolyte indicates electrochemical and photoelectrochemical processes related to CO_2, it is essential to emphasize that CV data alone cannot prove or confirm the formation of specific CO_2 reduction products (such as methanol, ethanol, or carbon monoxide) [20]. In electrochemical systems, faradaic current peaks can be indicative of various interfacial reactions. Definitive confirmation of product identity and faradaic efficiency requires quantitative post-electrolysis chemical analysis, such as gas chromatography (GC), proton nuclear magnetic resonance (^{1}H NMR), or high-performance liquid chromatography (HPLC) [20,22,23].

3. Conclusions

ZnO nanoparticles were successfully synthesized via a facile sol-gel method under an inert N_2 atmosphere. Post-synthetic thermal annealing systematically increased the crystallite size from 3.23 nm to 19.33 nm while preserving the stable hexagonal wurtzite phase. FTIR analysis confirmed progressive surface dehydroxylation through the condensation of surface-bound hydroxyl groups and clarified that the residual bands at 1582 cm^{-1} and 1340 cm^{-1} originate from precursor-derived bridging carboxylate and weakly bound acetic acid species, rather than from isolated carbonyl stretching vibrations. SEM observations revealed a progressive transition toward a more uniform distribution of quasi-spherical agglomerates, with the apparent particle size decreasing to 32.5 ± 4.8 nm at 450°C.

Nitrogen annealing at 450°C promoted the formation of point defects, wherein thermal desorption of lattice oxygen anions under oxygen-deficient conditions created stable surface oxygen vacancies (V_o). This was initially evidenced by the oxygen deficiency

observed in EDS atomic ratios ($ZnO_{0.77}$) and further corroborated by the dominant green-yellow visible emission in room-temperature PL spectra. These oxygen vacancies introduced localized sub-bandgap states, resulting in a marginal band gap decrease from 3.33 eV to 3.30 eV (UV-Vis) and acting as charge-trapping states that suppress fast carrier recombination.

Photoelectrochemical CV testing in N_2-saturated electrolyte exhibited a featureless capacitive response, confirming electrode stability. In CO_2-saturated unbuffered Na_2SO_4, unassisted local surface alkalization ($pH_{lo}c_{al} > 9$) and CO_2 activation polarization shifted the reduction potentials cathodically. A significant enhancement in cathodic current density was confirmed for the ZnO 450 electrode under UV illumination, increasing from -0.0334 mA cm^{-2} to -0.0747 mA cm^{-2}. This enhanced photo-response is attributed to oxygen-vacancy-mediated charge separation and improved interfacial electron transfer, underscoring the critical role of defect engineering in enhancing the photoelectrochemical CO_2 reduction performance of ZnO. Conversely, the ZnO 300 electrode exhibited an anomalous decrease in cathodic current under illumination (from -0.0881 mA cm^{-2} to -0.0709 mA cm^{-2}), attributed to rapid charge recombination at residual acetate/carboxylate surface states and the insufficient presence of oxygen vacancy trapping channels.

Acknowledgments

This work was partly supported by BUPP contract number 977/UN6.3.1/PT.00/2025 dated 16th April 2025 and by Universitas Padjadjaran through the Indonesian Endowment Fund for Education (LPDP) on behalf of The Indonesian Ministry of Higher Education, Science and Technology and Managed under the EQUITY Program (Contract No. 4303/B3/DT.0308/2025 and 3972/UN6.RKT/HK.07.00/2025).

References

1. Wang J and Azam W 2024 Natural resource scarcity, fossil fuel energy consumption, and total greenhouse gas emissions in top emitting countries Geosci. Front. 15
2. Yusuf M and Ibrahim H 2023 A comprehensive review on recent trends in carbon capture, utilization, and storage techniques J. Environ. Chem. Eng. 11
3. Chen S, Abdel-Mageed A M, Hauble A, Ishida T, Murayama T, Parlinska-Wojtan M and Behm R J 2021 Performance of Au/ZnO catalysts in CO2 reduction to methanol: Varying the Au loading / Au particle size Appl. Catal. A Gen. 624
4. Pawar, Amol U.; Kim, Chang Woo; Nguyen-Le, Minh-Tri; Kang Y S 2019 General Review on the Components and Parameters of Photoelectrochemical System for CO2 Reduction with in Situ Analysis ACS Sustain. Chem. Eng. 7 7431–55
5. Yang, Jinghai; Liu, Xiaoyan; Yang, Lili; Wang, Yaxin; Zhang, Yongjun; Lang, Jihui; Gao, Ming; Feng B 2009 Effect of annealing temperature on the structure and optical properties of ZnO nanoparticles J. Alloys Compd. 477 632–5
6. Chen, Yi; Nayak, Jyoti; Ko, Hyun-U; Kim J 2012 Effect of annealing temperature on the characteristics of ZnO thin films J. Phys. Chem. Solids 73 1259–63
7. Ng, Zi-Neng; Chan, Kah-Yoong; Tohsophon T 2012 Effects of annealing temperature on ZnO and AZO films prepared by sol–gel technique Appl. Surf. Sci. 258 9604–9

8. Zong X, Jin Y, Li Y, Zhang X, Zhang S, Xie H, Zhang J and Xiong Y 2022 Morphology-controllable ZnO catalysts enriched with oxygen-vacancies for boosting CO2electroreduction to CO J. CO2 Util. 61
9. Lim W C, Singh J P, Kim Y, Song J, Chae K H and Seong T Y 2021 Effect of thermal annealing on the properties of ZnO thin films Vacuum 183
10. Bui, Quang Chieu; Salem, Bassem; Roussel, Hervé; Mescot, Xavier; Guerfi, Youssouf; Jiménez, Carmen; Consonni, Vincent; Ardila G 2021 Effects of thermal annealing on the structural and electrical properties of ZnO thin films for boosting their piezoelectric response J. Alloys Compd. 870
11. Umar, Ahmad; Kumar, Rajesh; Kumar, Girish; Algarni, H.; Kim S H 2015 Effect of annealing temperature on the properties and photocatalytic efficiencies of ZnO nanoparticles J. Alloys Compd. 648 46–52
12. Suguna A, Prabhu S, Selvaraj M, Geerthana M, Silambarasan A, Navaneethan M, Ramesh R and Sridevi C 2022 Annealing effect on photocatalytic activity of ZnO nanostructures for organic dye degradation J. Mater. Sci. Mater. Electron. 33 8868–79
13. Ghosh B and Ghosh R 2026 Effect of ZnO seed layer annealing for growth of oriented ZnO nano columns towards superior ultra-violet detection Thin Solid Films 836
14. Verma N, Rakhra M, Bhatt M W and Garg U 2022 Engineering technology characterization of source solution for ZnO and their data analytics effect with aloe vera extract Neurosci. Informatics 2
15. Mallika A N, Reddy A R and Reddy K V 2015 Annealing effects on the structural and optical properties of ZnO nanoparticles with PVA and CA as chelating agents J. Adv. Ceram. 4 123–9
16. Khan M R, Abushad M, Ahmed H, Husain S and Khan W 2025 Study of polaron hopping conduction mechanism and dielectric behavior of ZnO nanostructures synthesized via hydrothermal method at different temperatures J. Mater. Sci. Mater. Electron. 36 1–17
17. Rafaie H A, Dasiano S H N I, Kasim M F, Ramli N I T, Hir Z A M and Mamat M H 2022 CONSTRUCTING NI-DOPED ZnO/GO HETEROSTUCTURES FOR ENHANCED SUNLIGHT-TRIGGERED DEGRADATION OF METHYLENE BLUE DYE Malaysian J. Anal. Sci. 26 520–31
18. Kut D, Mariychuk R, Pogodin A and Kut M 2026 Experimental and theoretical approach to determining the nature of energy transitions in linear halogen- and chalcogen-functionalized derivatives of thiazolo[2,3-b]quinazolines Chem. Phys. 604
19. Rashid A R A, Hazwani T N, Mukhtar W M and Taib N A M 2018 Influence of annealing temperature on optical properties of Al doped ZnO nanoparticles via sol-gel methods AIP Conf. Proc. 1972
20. Alvim J C, Carvalho Soares L, Macedo N G, Tayar Galante M, Sangali M, Caram R, de Siervo A, Chansai S, Hardacre C and Longo C 2025 Unassisted Photoelectrochemical CO2 Conversion into Liquid Products by a Light-Responsive Gas-Diffusion Electrode ACS Sustain. Chem. Eng. 13 8988–98
21. Abdolmohammadi S, Afsharpour M and Keshavarz-Fatideh S 2014 An efficient green synthesis of 3-amino-1H-chromenes catalyzed by ZnO nanoparticles thin-film South African J. Chem. 67 203–10

22. Robens E, Hecker B, Kungl H, Tempel H and Eichel R A 2023 Bimetallic Copper-Silver Catalysts for the Electrochemical Reduction of CO2 to Ethanol ACS Appl. Energy Mater. 6 7571–7
23. Hecker B, Robens E, Valencia H E, Windmüller A, Muench F, Meledina M, Tempel H, Kungl H, Mayer J and Eichel R-A 2023 Effects of Synthesized Silver Nanoplate Structures on the Electrochemical Reduction of CO 2 J. Electrochem. Soc. 170 096505
24. Wang J, Zhang T, Liu X, Yang L, Cao J, Wu Q, Wang F, Chen Y, Li X and Wei M 2025 Fabrication of a 3D/0D S-scheme heterojunction based on ZnO nanoflowers and ZnIn 2 S 4 nanoparticles with enhanced CO 2 photoreduction performance RSC Adv. 15 40174–87
25. Wang J-X, Lin H Y, Tu K-Y and Wu J M 2026 Defect-Tailored ZnO Nanoflowers Enable Efficient, Metal-Free Ammonia Synthesis through Coupled Piezoelectric and Photocatalytic Activation J. Mater. Chem. A 2 10633–45